

THE LEAD GLASS COLUMNS

A LARGE SHOWER DETECTOR AT THE SLAC HYBRID FACILITY

J. E. Brau<sup>7</sup>, J. Butler<sup>7</sup>, W. M. Bugg<sup>11</sup>, J. T. Carroll<sup>7</sup>, C. V. Cautis<sup>7</sup>,  
H. O. Cohn<sup>5</sup>, G. Condo<sup>11</sup>, S. Dado<sup>8</sup>, F. Davenport<sup>2</sup>, R. Diamond<sup>2</sup>,  
R. Erickson<sup>7</sup>, M. Ferguson<sup>1</sup>, R. C. Field<sup>7</sup>, L. R. Fortney<sup>1</sup>, B. Franek<sup>6</sup>,  
R. Gearhart<sup>7</sup>, T. Glanzman<sup>1</sup>, J. Goldberg<sup>8</sup>, A. T. Goshaw<sup>1</sup>, V. Hagopian<sup>2</sup>,  
T. Handler<sup>11</sup>, H. J. Hargis<sup>11</sup>, E. Hart<sup>11</sup>, D. Q. Huang<sup>4†</sup>, D. P. Kelsey<sup>6</sup>,  
J. Lannutti<sup>2</sup>, P. W. Lucas<sup>1</sup>, K. C. Moffeit<sup>7</sup>, T. Maruyama<sup>10</sup>,  
A. P. T. Palounek<sup>1</sup>, D. B. Parker<sup>7</sup>, A. Rafatian<sup>11</sup>, W. J. Robertson<sup>1</sup>,  
A. H. Rogers<sup>11</sup>, R. Sugahara<sup>3</sup>, K. Takahashi<sup>3</sup>, S. Tether<sup>4</sup>, W. D. Walker<sup>1</sup>,  
A. Yamaguchi<sup>9</sup>, and R. K. Yamamoto<sup>4</sup>.

ABSTRACT

A large lead glass shower detector containing 204 lead glass blocks and 250 finger hodoscope elements has been constructed and operated in a photoproduction experiment at the SLAC Hybrid Facility. An energy resolution of  $\sigma_E/E = (0.84 + 4.8/\sqrt{E})\%$  has been achieved for electron energies between 4 and 16 GeV. Details of the apparatus, its stability monitoring system, and its use in triggering the bubble chamber are presented. The performance of the detector in electron identification and  $\pi^0$  reconstruction is discussed.

Submitted to Nuclear Instruments and Methods

---

† On leave of absence from the Institute of High Energy Physics, Beijing, China.

- 1 Duke University, Durham, North Carolina, USA.
- 2 Florida State University, Tallahassee, Florida, USA.
- 3 KEK, Oho-Machi, Tsukuba-gun, Ibaraki, Japan.
- 4 Massachusetts Institute of Technology, Cambridge, Massachusetts, USA.
- 5 ORNL, Oak Ridge, Tennessee, USA.
- 6 Rutherford and Appleton Laboratories, Didcot, England.
- 7 SLAC, Stanford University, Stanford, California, USA.
- 8 Technion-Israel Institute of Technology, Technion City, Haifa, Israel.
- 9 Tohoku University, Sendai, Japan.
- 10 Tufts University, Medford, Massachusetts, USA.
- 11 University of Tennessee, Knoxville, Tennessee, USA.

## I. INTRODUCTION

A large lead glass shower detector (the Lead Glass Columns) has been constructed and operated in a photoproduction experiment at the SLAC Hybrid Facility [1]. This paper describes the detector and details its performance characteristics in this experiment.

Section II describes the experiment in which this detector is being used and section III the geometrical configuration of the lead glass itself. Section IV presents the data acquisition system, including the triggering, digitization, and stability monitoring subsystems. The calibration procedures and a discussion of energy and position resolution are given in section V. The performance of the detector in electron identification and  $\pi^0$  detection is detailed in sections VI and VII, and section VIII presents a summary of the work.

## II. THE PHOTOPRODUCTION EXPERIMENT

The experiment (SLAC BC 72/73) employs a backscattered laser beam [2] to produce 20 GeV/c photons at the SLAC 40-inch hydrogen bubble chamber. Figure 1 illustrates the photon beam. A neodymium-YAG laser is frequency quadrupled to produce about 100 millijoules of 4.68 eV photons which are directed into the primary 30 GeV/c electron beam of the linac. These photons are backscattered to produce a 60 nanosecond pulse of 20 to 25 linearly (or circularly) polarized photons which are collimated to 10 microradians at the bubble chamber, yielding a 2 GeV FWHM photon energy spectrum (see fig. 2).

The primary physics objectives of the experiment are studies of photoproduced charm particles and higher mass vector mesons.

The standard bubble chamber cameras have been augmented with a high resolution camera for the detection of charm decay vertices. The bubble chamber is operated in the high bubble density mode and photographs of 55 micron diameter bubbles are taken with the high resolution camera about 150 microseconds following beam time. The SLAC Hybrid Facility provides detectors downstream of the bubble chamber in the form of proportional wire chambers, Cerenkov counters, and the lead glass shower detector (fig. 3). The downstream detectors (including the lead glass) provide the trigger for the bubble chamber flash lamps which results in better than one hadronic event in every four pictures taken.

### III. PHYSICAL LAYOUT

This detector has evolved from two previous experiments at SLAC: the MARK I/Lead Glass Wall experiment [3] at SPEAR and the 16 GeV/c  $\pi^+p$  Duke/Florida State/Oak Ridge/SLAC/SUNY/Tennessee Lead Glass Wall experiment (BC-67) [4] at the SLAC Hybrid Facility. Since the completion of BC-67, the detector has been rebuilt with new hodoscopes and electronics to be suitable for the current experiment. In the present structure, the lead glass has been configured with a variable width gap splitting the detector into a north and a south half. This design allows the photon beam and its associated pair conversion electrons (having been spread in the vertical plane by the field of the bubble chamber magnet) to pass through the detector without interacting. The variable gap can be closed to five millimeters and opened to more than 35 centimeters. Operation to date has been with an 11 centimeter gap.

Figure 4 shows the layout of the Lead Glass Columns. The detector consists of a filter hodoscope, a lead shield, an active converter, two planes of finger hodoscopes, and an array of back blocks. Its basic structure of a scintillator hodoscope situated between an active converter and an array of absorbing back blocks is similar to the design used in previous fixed target experiments [5]. It sits about 6.4 meters from the center of the bubble chamber with an active area of about 3.3 square meters, covering .08 steradians of the solid angle from the bubble chamber. This geometry provides good detection efficiency over most of the forward hemisphere (Feynman  $x > 0.1$ ) for the current 20 GeV  $\gamma p$  experiment. Particles enter the detector through the 24-cell filter hodoscope, designed to discriminate between gammas which convert upstream of the lead glass detector from those entering the lead glass unconverted. Those gammas which convert in the exit windows (.115 radiation lengths) of the bubble chamber and its vacuum chamber, for example, send an electron and a positron which are separated by the field of the bubble chamber magnet into the downstream system. Each paddle of the filter hodoscope is a 22 centimeter high by 60 centimeter wide by .64 centimeter thick piece of NE102. A simple light guide brings the light from each paddle into an Amperex 56AVP photomultiplier tube.

Ten centimeters behind the filter hodoscope hang two sheets of 0.64 centimeter (1.13 radiation lengths) thick lead. Each sheet is sandwiched between two sheets of 0.16 centimeter thick aluminum. These sheets, referred to as the lead shield, stretch 290 centimeters high and 63 centimeters wide, one on each side of the beam gap, suspended from above, and braced at the bottom to prevent motion.

The lead shield reduces the fraction of high energy gammas which pass through the active converter unconverted and increases the flux of electrons from converted gammas passing through the finger hodoscope. A Monte Carlo calculation demonstrated that this shield contributes in quadrature a term of  $\sigma/E = 1.5\%/E$  (GeV) to the inherent energy resolution.

Two and one-half centimeters behind the lead shield is the front face of the active converter. On each side of the beam gap stands a column of 26 lead glass blocks sitting 4.1 centimeters off the detector floor on a piece of aluminum channel. The active converters are held in place by two vertical beams and a sheet of 0.16 centimeter thick aluminum wrapped around the glass and attached to the vertical beams. The 26 active converter blocks on each side of the detector are 90 centimeters wide, ten centimeters thick (3.3 radiation lengths), and 285 centimeters high (10.9 centimeters per block). Each block is viewed by an EMI 9531R 3.5 inch photomultiplier tube. These active converter blocks are Schott type F2 lead glass, as are the back blocks. Table I summarizes the properties of the glass.

Behind the active converter sits the finger hodoscope. This hodoscope consists of 250 NE114 scintillator fingers 2.5 centimeters wide, 1.3 centimeters thick, each viewed by an RCA931A photomultiplier tube. The 274 centimeter long vertical fingers are directly behind the active converter, 23 on each side of the beam gap. Behind the vertical fingers stretch 204, 61 centimeter long horizontal fingers, 102 on each side of the beam gap. This finger hodoscope sits as close as possible to the active converter.

The lead glass absorber, an array of 152 "back blocks," sits behind the finger hodoscope. The front face of the back blocks is 16.5 centimeters behind the back surface of the active converter. This is the shortest distance which permits installation of the finger hodoscope. These back blocks are stacked in eight columns, four on each side of the beam gap, with 19 blocks in each column. Each block has a 15.3 centimeter by 15.3 centimeter cross section. The top and bottom four rows of each column consist of blocks 32.2 centimeters deep (10.5 radiation lengths) while the central 11 rows have twice this depth (64.4 centimeters or 21 radiation lengths) formed by gluing two 32.2 centimeter long blocks end to end. Each of these back blocks is viewed by an EMI 9618R 5-inch photomultiplier tube mounted horizontally on the back of the block. The back blocks are partially supported by an aluminum wrapper which introduces 0.16 centimeters of aluminum at the front face and along the side adjacent to the beam gap.

This entire lead glass detector is enclosed in a light tight, air conditioned box maintained at 22 degrees centigrade with a stability of plus or minus one degree. Temperature stability is crucial since the phototube response varies about one percent per degree centigrade, and the monitoring system to be described later relies on a light emitting diode which has a negative one-half percent per degree centigrade temperature dependence. The temperature is monitored continuously and recorded on magnetic tape along with the data.

The photomultiplier tubes are powered by seven LeCroy 4032 and nine LeCroy 4032A 32-channel high voltage power supplies which are controlled and monitored by a Data General NOVA 4X computer through a CAMAC system.

#### IV. DATA ACQUISITION

The signals from each of the lead glass and finger hodoscope photomultiplier tubes are transported 35 meters on RG-174 coaxial cables for digitization on the Brilliant ADC [6] / SHAM IV [7] system. Figure 5 illustrates this arrangement. Each photomultiplier tube is attached to one of the 32 channels in a SHAM IV (sample and hold) module which integrates the pulse for 400 nanoseconds at beam time (the 60 nanosecond long beam pulse comes at the rate of 10 Hertz). Then, the BADC steps through the SHAM IV channels, digitizing to 12-bit accuracy [8] each of the channels in sequence. To do this the Brilliant ADC (BADC) directs via CAMAC instructions, through the SHAM interface module [9], a specific channel in the SHAM IV crate to set a voltage level proportional to the integrated pulse height for that channel. Digitization takes two microseconds per channel and, with the 200 nanosecond BADC microprocessor cycle time, it takes about four microseconds per photomultiplier channel to process the data. The digitization is performed twice for each beam spill. The first is a fast pass where channels below specified thresholds are ignored, and channels above are converted to energy units, making energy measurements available to the host computer in less than a millisecond for trigger decisions (these measurements are not used in the current experiment). During this first pass, only the lead glass signals are digitized. Several milliseconds later all channels are digitized and retained (i.e., no threshold cuts are applied) to be recorded on magnetic tape.

The dynode signals from the photomultipliers are used to obtain a fast (less than 1  $\mu$ sec), on-line measurement of the energy deposited in various sections of the lead glass. For the present experiment, the dynode voltage pulses from the photomultipliers in the north active converter column, the south active converter column, the north back block column, and the south back block column are separately summed using fast linear analog adders. After amplifying by a factor of 10, these signals are discriminated at voltage levels corresponding to desired energy thresholds. If the energy deposited in any of the four columns exceeds its threshold, the bubble chamber cameras are triggered. Figure 6 shows the probability of generating a trigger from a given column as a function of the energy deposited in the lead glass of that column. The thresholds for triggering the active converter columns have been set at about 800 MeV while the threshold for each back block column is 2.0 GeV. Of the triggers taken, about 35 percent are triggered on the back blocks only, 30 percent on the active converters only, and the remaining 35 percent are triggered on both back blocks and active converters. The pictures taken with the lead glass trigger have a hadronic event in the 75 centimeter long bubble chamber fiducial volume about 29 percent of the time. The lead glass triggers on about 85 percent of the hadronic events recorded (the remainder comes from a 168E microprocessor [10] track finding algorithm based on hits in the proportional wire chambers). The experiment triggers on about 90 percent of the hadronic cross section, meaning the lead glass triggers on about 76 percent.

The pulses from the filter hodoscope are recorded as latches on two LeCroy CAMAC Module 2340B 16-channel discriminator coincidence registers.

A program on the NOVA 4X computer reads and controls the LeCroy 4032/4032A high voltage power supplies. Two LeCroy 2132 High voltage interface modules are used to tie the power supplies to the NOVA 4X. Periodically during the run, all the voltages are read and compared with a standard voltage table stored on a disk file. If the voltage on any channel differs from its standard by more than its tolerance, the operator is informed and directed to correct the condition. The lead glass voltages are allowed to differ by one volt, the finger hodoscope voltages by five volts, and the filter hodoscope voltages by ten volts. After the high voltage comparison, the voltages are recorded on magnetic tape.

The system developed by the LBL-SLAC MARK I Lead Glass Wall collaboration [11] to monitor the lead glass was installed in the new detector with one modification. A single high-intensity light-emitting diode (LED), a Monsanto MV5352, sends test pulses to each lead glass block through a bundle of low-attenuation plastic optical fiber cables (DUPONT PPX-0715). The 60 Hertz relay pulser described by Madaras et al., was replaced by a faster control module to permit efficient pulsing of the system between beam spills. The intensity of the light seen varies from counter to counter, but typically it is a large fraction (many tens of percent) of the dynamic range of the digitizer. The LED's are flashed between beam spills at a frequency of one flash per 500 beam spills (about once a minute).

The intensity of the LED itself is monitored by three reference counters, which also measure light from radioactive sources consisting of Americium-241 (Am-241) diffused in NaI crystals. In actual practice the Am-241 data have not been used due to the good stability of the phototubes and the LED.

Between the LED and the fiber bundle is a filter wheel which allows twelve differing levels of transmission of the light to the photomultiplier tubes. Normally this wheel is set to the 100 percent transmission position, but periodically (every few days) the filter wheel is stepped through its twelve positions and data are collected for each position. The pulse heights observed at the 20 percent transmission position of the filter wheel were multiplied by five to obtain an expected value for 100 percent transmission. Figure 7 shows the ratio of the observed pulse height to this expected value against the observed 100 percent transmission pulse height. A clear nonlinearity is seen as the lower pulse heights scale nicely between 20 percent and 100 percent transmission, while the larger pulse heights do not. The data for all twelve filter wheel positions were used to obtain a fit (shown on Figure 7) to the pulse height measured for a given expected pulse height:

$$I_p = I_m (1 + 1.1045 \times 10^{-6} I_m + 6.58 \times 10^{-11} I_m^2)$$

where  $I_p$  is the predicted (or expected) pulse height and  $I_m$  is the measured pulse height. This correction has been applied to all the raw data measurements.

A few times a day the LED generated signals and the ADC pedestals on each channel are examined by a NOVA program and compared with a set of standards on a disk file. In the event of any discrepancies, the operator is notified to take action.

## V. ENERGY CALIBRATION AND POSITION RESOLUTION

The lead glass blocks are calibrated with an electron beam that is sent through the empty bubble chamber into the lead glass. The entire detector was calibrated at 4 GeV and a subset of blocks were also used to measure 8, 12, and 16 GeV electron showers. The 4 GeV electrons were injected into each of the back blocks by moving the entire detector sideways on tracks until the electrons were centered on the appropriate column and setting the field of the bubble chamber magnet until they were centered on the selected row. The beam, consisting of approximately 80 percent electrons, was run allowing about one-half particle per 1.5 microsecond pulse to reach the lead glass. A pile-up veto rejected pulses for which two or more particles were detected in the trigger scintillator upstream of the bubble chamber. Up to 3,000 triggers were recorded on magnetic tape for each back block.

Good electron showers were selected off line from this data. Figure 8 shows the energy measured in the active converter, the back blocks, and the sum for a typical back block run, before any selection. The pions and muons in the beam were removed by requiring a sizeable energy deposit (typically about 400 MeV) in the active converter. Electrons which lose energy upstream as they are transported to the detector are deflected from the selected back block by the bubble chamber magnetic field. Events with energy in the active converter above or below the three active converters in the intended region or in which the largest back block energy did not appear in the targeted block were rejected. After this selection of events, an iterative procedure was used to calculate calibration constants which relate pulse height to energy for each block. Starting with an assumed set of initial

coefficients, a fit was computed for each of the 152 electron data runs (one for each back block.) These fits consist of minimizing the  $\chi^2$  defined by

$$\chi^2 = \sum_{i=1}^k (E - \sum_{j=1}^n C_j P_{ij})^2$$

where E is the electron energy,  $C_j$  is the energy coefficient for block j and  $P_{ij}$  is the pulse height for block j on event i. For each run, all blocks contributing one-half a percent of the total energy were included in the fit, but only those coefficients for blocks contributing five percent of the energy were free to change in the fit. After all the runs were fitted, the resulting values were used as the assumed coefficients for the next iteration. Convergence was found in a few iterations. Figure 9 is a histogram of the energy coefficients for the blocks. The voltages on the tubes have been set to balance dynode responses, in order to optimize the trigger energy threshold. In addition the gains of the photomultipliers attached to the active converters, single back blocks, and double back blocks were set to different values in order to best match the maximum energy deposited in each of these sections to the dynamic range of the BADC system.

Figure 10 shows the root-mean-squared deviation of the energy distribution for each of the 152 runs using the final set of energy coefficients. Figure 11 shows the energy distribution for approximately 100 arbitrary events from each of the 152 runs. This shows an overall resolution of 3.7 percent over the entire detector.

Figure 12 shows a set of four measurements which were performed on one block at 4, 8, 12, and 16 GeV. The energy distributions for each of

these runs were obtained by applying the energy coefficients determined by the 4 GeV run. Figure 13 summarizes these data showing that the coefficients determined with the 4 GeV beam gave good resolution up to 16 GeV with a nonlinearity of about 2.5 percent at 16 GeV. A fit to the energy dependence of the resolution shown in Figure 13 yields:

$$\frac{\sigma}{E} = (0.84 + 4.8/\sqrt{E})\% \quad .$$

A study was conducted to determine systematic measurement errors for low energy photons. Photon showers were simulated with the EGS electromagnetic cascade shower simulation program [12]. The total electron track length, weighted for the Cerenkov light dependence on  $\beta$ , was calculated and multiplied by the energy coefficients. Figure 14 shows the ratio of this calculation of measured energy to actual photon energy as a function of photon energy. We have included a correction factor in our shower program for gammas below 1 Gev to account for this effect.

The centroid of pulse heights on the finger hodoscope was used to determine the position of a shower. During a calibration run electron trajectories were measured in two millimeter spaced proportional wire chambers located 4.4 and 5.2 meters in front of the finger hodoscope. With these chambers, the electron coordinates at the finger hodoscope were determined to an accuracy of five millimeters. Figure 15 shows the difference between the measured position for a run of 4 GeV electrons and the predicted horizontal and vertical positions from the proportional wire chambers. The distributions have standard deviations of 8.8 and 9.9 millimeters, implying, based on the 5 millimeter PWC

resolution, that the 4 GeV shower positions are determined to 7.2 and 8.5 millimeters.

## VI. ELECTRON IDENTIFICATION

Electron identification is accomplished by a combination of requirements on energy in the lead glass blocks and pulse heights in the finger hodoscope. In order to study the level of pion rejection provided by these requirements we conducted a test using 8 GeV pions. Figure 16 shows the distribution of energy deposited in the lead glass for pions incident within a one inch-square scintillator mounted on the front of the detector. The test was done at two locations, one entering a double back block and the other a single back block. Two sets of cuts were developed to reject pions. The variables used were the total deposited energy, the energy in the active converter, the distance of the shower center from the beam center, and the second moment  $M_2$  of the pulse height distribution in the finger hodoscope:

$$M_2 = \left[ \sum i^2 P_i - (\sum iP_i)^2 / \sum P_i \right] / \sum P_i$$

where  $P_i$  is the pulse height in finger  $i$ .

The last two variables discriminate between electromagnetic and hadronic showers originating in the active converter in that the hadronic showers tend to be broader, resulting in larger observed deviation from the beam and a larger second moment. Table II presents the results of the two sets of cuts, one "hard" set designed to strongly reject pions with 50 percent electron rejection, and a "soft" set designed to retain 80 percent of the electrons with good pion

rejection. The hard cut requires 1.5 GeV in the active converter, a total energy between 7.6 and 8.4 GeV ( $\pm 5\%$ ), the shower center within 1.5 centimeters of the center of the incident beam and a second moment of less than 0.7 in the y-coordinate (the bubble chamber field bend direction) and 0.5 in the z-coordinate. The soft cut requires 1.0 GeV in the active converter, a total energy between 7.4 and 8.6 GeV ( $\pm 7.5\%$ ), a shower center within 1.7 centimeters of the incident beam and a second moment of less than 1.0 in y and 0.7 in z. Clearly from table II, misidentification on the order of only  $10^{-4}$  for pions is achieved with about 50 percent electron survival, while only  $10^{-3}$  pion misidentification is achieved with 80 percent electron survival. In the experiment, particle momenta are measured in the bubble chamber-proportional wire chamber system, and compared to the energy measurement in the lead glass. This large electron/pion discrimination factor will permit the identification of semileptonic charm decays observed directly in the bubble chamber.

#### VII. PI ZERO DETECTION

The lead glass data are analyzed off-line with a pattern recognition program which searches in the back blocks and the active converters for clusters of energy. Each cluster is defined by a local maximum. If two maxima can be identified in a small region of the detector, two clusters will be defined. The program matches the back block and active converter clusters which are consistent with the same shower pointing to the primary vertex in the bubble chamber. Next, peaks in the finger hodoscope are associated with showers. Finally, the filter hodoscope in front of each shower is examined. If it is on, that

shower is flagged. After all the showers are located, the charged tracks from the bubble chamber are projected into the lead glass and used to identify charged showers in the lead glass.

Figure 17 shows the mass distribution for all two-shower combinations after showers originating directly from charged tracks observed in the bubble chamber are removed. The pi zero signal is obvious, but it sits on a large background. The background is due to several factors, the most significant being muons from the accelerator, secondary hadronic interactions, and showers developing in the edges of the active converter. Figure 18 shows the mass plot for these same events, but now only showers which are seen in both the horizontal and vertical hodoscopes are included. The pi zero signal is now much more prominent. The number of events in the pi zero region (120-150 MeV/c<sup>2</sup>) is nearly the same for figures 17 and 18, leading to the conclusion that the requirement of both finger hodoscopes is an efficient one for selecting well measured gammas from the bubble chamber events.

Figure 19 shows the result of using the filter hodoscope to further remove background. Here we have removed pairs if one of the gammas has less than 1 GeV of energy and it has a hit in the filter hodoscope (higher energy gammas have an increasing probability to send electrons back into the hodoscope as they begin to shower in the lead shield). The background is reduced by about a factor of two while the pi zero signal suffers little degradation.

Figure 20 shows the combinations in figure 19, plotted as a function of the number of gammas seen in the detector. Clearly the background increases, as it should, as the number of gammas increases. Figure 21 shows the two-gamma mass plot for various two-gamma

energies. The mass resolution of about 10 MeV/c exhibits a slight energy dependence.

The gammas detected in the lead glass have been combined with measured charged tracks in the bubble chamber-proportional wire chamber system. Figure 22 shows the mass for  $\pi^+\pi^-\pi^0$  combinations where the laboratory momentum for this three pion system exceeds 12 GeV/c. The measured pi zero has been constrained to the pi zero mass by the program SQUAW to improve its measured quantities. From this plot we see a three pion mass resolution in the omega meson region of about 17 MeV/c<sup>2</sup>.

#### VIII. SUMMARY

A large lead glass shower detector has been constructed and operated in a photoproduction experiment at the SLAC Hybrid Facility. The detector has an energy resolution varying from 3.3 percent at 4 GeV to 2.1 percent at 16 GeV and a spatial resolution of 7-8 millimeters for electron induced electromagnetic showers. Near the  $\pi^0$  mass we observe a two gamma mass resolution of about 10 MeV/c<sup>2</sup>. The gammas detected in the lead glass can be combined with charged tracks that are measured using a bubble chamber-proportional wire chamber system. Using this combined hybrid facility, we measure a mass resolution of about 17 MeV/c for the  $\pi^+\pi^-\pi^0$  system at the omega meson mass. The lead glass shower detector can also be used to rather clearly identify electrons. A selection algorithm has been developed which accepts 50 percent of 8 GeV electrons with a  $10^{-4}$  pion misidentification probability or accepts 80 percent with a pion misidentification probability of  $10^{-3}$ .

### Acknowledgements

We are indebted to the following people who contributed technical support during the construction and operation of this detector:

L. Barker, R. Belusevic, G. Cunningham, C. Cupp, D. Freytag, C. Hoard, C. McManus, J. Milward, A. Schinn, and W. Schutte.

This work was supported in part by the Department of Energy, contracts DE-AC03-76SF00515 (SLAC), E-(40-1)-3065 (Duke), EY-76-S-05-3509 (Florida State), DE-AC02-76ER03069 (MIT), W-7405-ENG-26 (ORNL), DE-AC02-76ER03023 (Tufts), DE-AS05-76ER03956 (Tennessee); by the Japan-US Cooperative Research Project on High Energy Physics under the Japanese Ministry of Education and the U. S. Department of Energy; and by the UK Science and Engineering Research Council.

REFERENCES

- [1] Ballam, J. and Watt, R. D., Ann. Rev. Nucl. Sci 27, 75 (1977);  
Field, R. C., SLAC SHF Note 67, December 1977.
- [2] This beam is similar to the lower energy beam described in  
Ballam, J., et al., Phys. Rev. D5, 545 (1972).  
A publication describing the current beam is in preparation.
- [3] Feller, J. M., et al., IEEE Trans. Nucl. Sci. 25, 304 (1977).
- [4] Lucas, P., et al., Bull. Amer. Phys. Soc. 25, 545 (1980).
- [5] Heller, M., et al., Nucl. Inst. and Methods 152, 379 (1978).
- [6] Breidenbach, M., et al., Proc. 1977 Nuclear Science Symposium,  
IEEE Transactions on Nuclear Science NS25, 706 (1978).
- [7] Cisneros, E., et al., 1980 Nuclear Science and Nuclear Power  
System Symposium, Orlando, Florida; SLAC-PUB-2641, October 1980.
- [8] The BADC provides data as 15-bit words with the least significant  
three bits always set to zero. Therefore, BADC counts or pulse  
heights in this paper refer to 15-bit words.
- [9] Brau, J. E. and Paffrath, L., SLAC Group-BC Internal Note  
#BC72-85, MARCH 1980.
- [10] Kunz, P.F., et al., Proc. 11th Annual Microprogramming Workshop SIGMICRO  
Newsletter 9, 25 (1978); Carroll, J. T., et al., SLAC-PUB-2726,  
contributed to the Topical Conference on Applications of Microprocessors  
to High Energy Physics Experiments, Geneva, Switzerland, May 4-6, 1981.
- [11] Madaras, R. J., Pardoe, B., and Pecyner, R., Nucl. Instru. and Methods  
160, 263 (1979).
- [12] Ford, R. L., and Nelson, W. R., SLAC-210, June 1978.

LIST OF TABLES

1. Properties of Schott F-2 Lead Glass
2. Electron Identification and Pion Misidentification Summary.

TABLE I

---

Properties of Schott F-2 Lead Glass

---

Density	3.6 gm/cm <sup>3</sup>
Composition	SiO <sub>2</sub> (46%) Na <sub>2</sub> (5%) K <sub>2</sub> O(4%) PbO(45%)
Index of Refraction	1.62
Radiation Length	3.06 cm
Hadronic Interaction Length	35 cm
Critical Energy	18 MeV

---

TABLE II

---

Electron Identification and Pion Misidentification

---

<u>Double Block Efficiency:</u>	<u>Electron</u>	<u>Pion</u>
Soft Cut	$0.77 \pm 0.04$	$(1.1 \pm 0.2) \times 10^{-3}$
Hard Cut	$0.44 \pm 0.04$	$(1.2 \pm 0.7) \times 10^{-4}$

---

<u>Single Block Efficiency:</u>	<u>Electron</u>	<u>Pion</u>
Soft Cut	$0.82 \pm 0.10$	$(1.5 \pm 0.2) \times 10^{-3}$
Hard Cut	$0.50 \pm 0.08$	$(1.5 \pm 0.8) \times 10^{-4}$

---

LIST OF FIGURES

- Fig. 1. Simplified representation of the backscattered laser beam.
- Fig. 2. The photon energy spectrum at the bubble chamber.
- Fig. 3. The SLAC Hybrid Facility.
- Fig. 4. Cut away view of the Lead Glass Columns.
- Fig. 5. The BADC/SHAM IV System.
- Fig. 6. The probability to trigger on the lead glass as a function of measured energy.
- Fig. 7. The ratio of the pulse height measured at 100 percent transmission to the pulse height expected based on the 20 percent transmission measurement, as a function of pulse height.
- Fig. 8. The energy measurements (a) in the active converter, (b) in the back blocks, and (c) the sum for 4 GeV incident electrons.
- Fig. 9. The energy gains for each of the lead glass channels.
- Fig. 10. The root-mean-squared deviation of the energy distributions for each of the 152 calibration runs.
- Fig. 11. The energy distribution for 4 GeV electron showers distributed over the Lead Glass Columns. Approximately one hundred random showers from each of the 152 runs are included.
- Fig. 12. The energy distribution for 4, 8, 12 and 16 GeV electrons.
- Fig. 13. The energy dependence of the energy resolution.
- Fig. 14. The average fraction of photon energy measured by the lead glass as a function of photon energy.
- Fig. 15. The position resolution of the finger hodoscope.

Fig. 16. Pion and electron total energy distributions.

Fig. 17. The two shower mass plot.

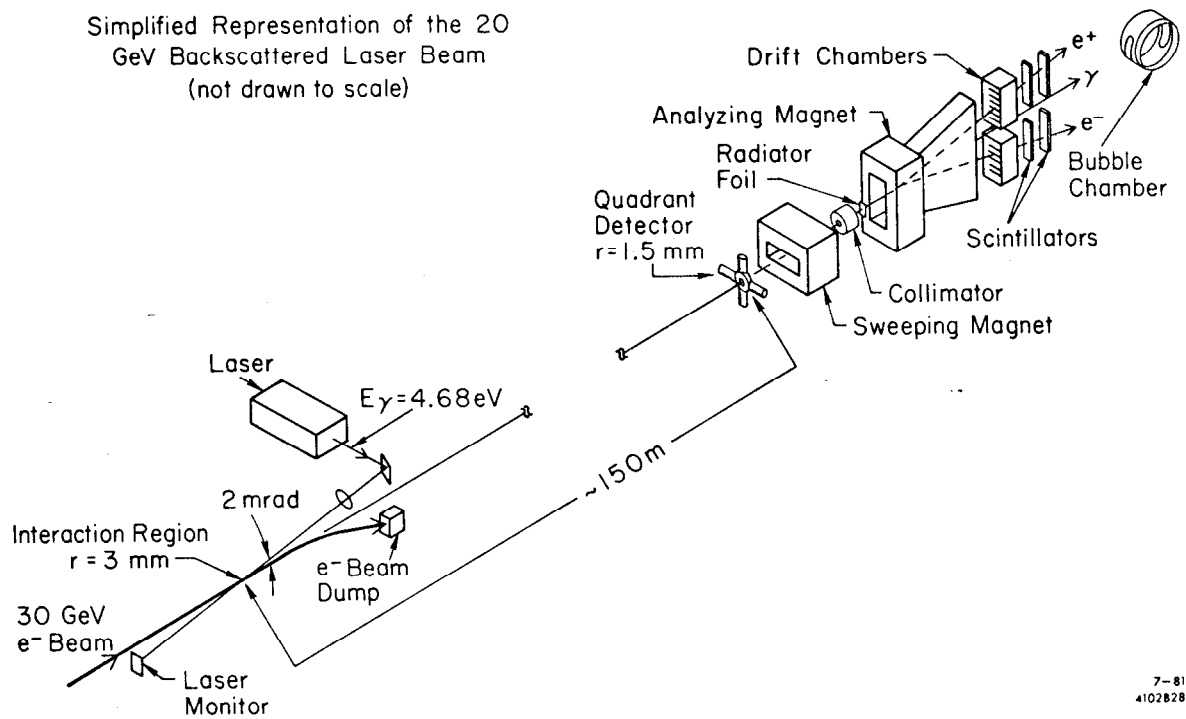
Fig. 18. The two gamma mass plot where the gamma is required to be detected in both finger hodoscopes.

Fig. 19. The two gamma mass plot after using the filter hodoscope veto on the gammas with less than 1 GeV energy.

Fig. 20. The two gamma mass plot for various gamma multiplicities:  
(a) 2 gamma, (b) 3 gamma, (c) 4 gamma, and (d) 5 gamma events.

Fig. 21. Two gamma mass plot for different two gamma energy ranges:  
(a) 2-4 GeV, (b) 4-6 GeV, (c) 6-8 GeV, and (d) 8-10 GeV.

Fig. 22. The  $\pi^+\pi^-\pi^0$  inclusive mass distribution for  
( $\pi^+\pi^-\pi^0$ ) momenta greater than 12 GeV/c.



7-81  
4102828

Fig. 1

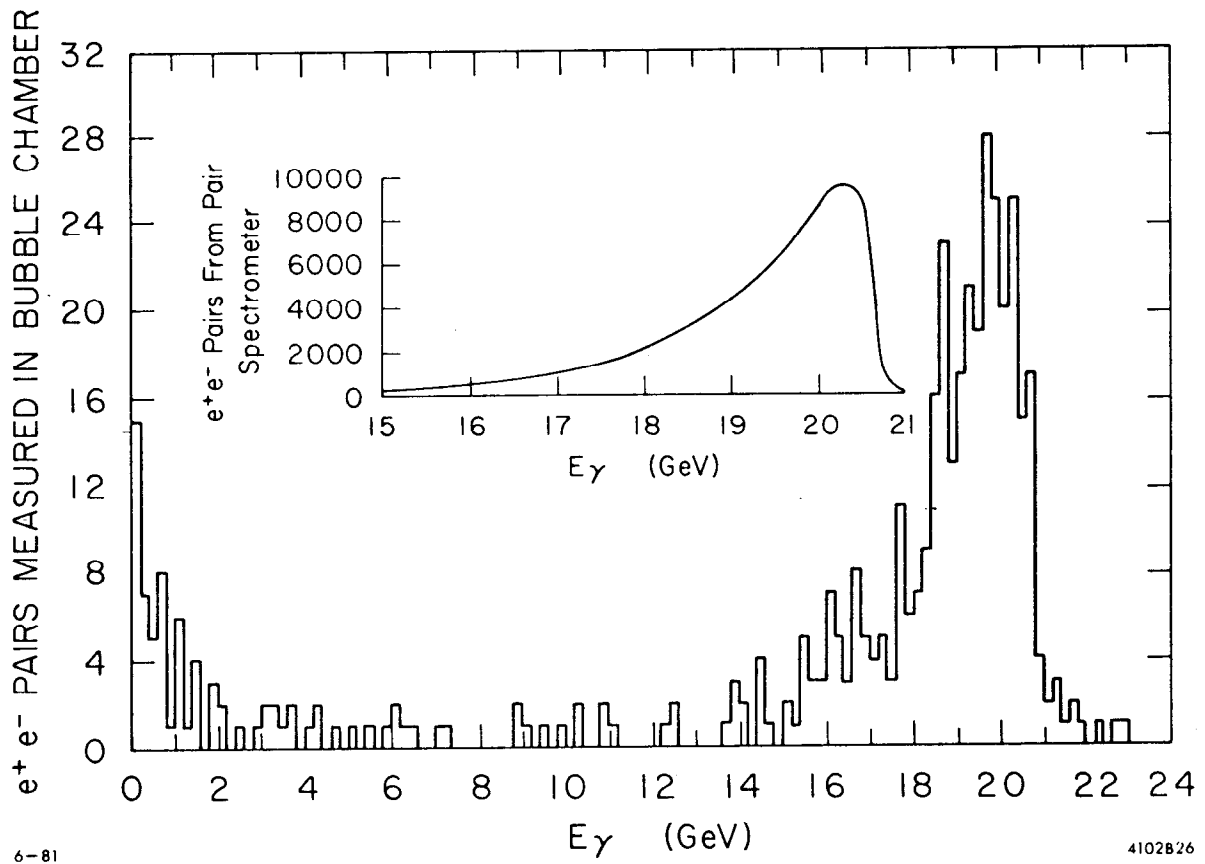
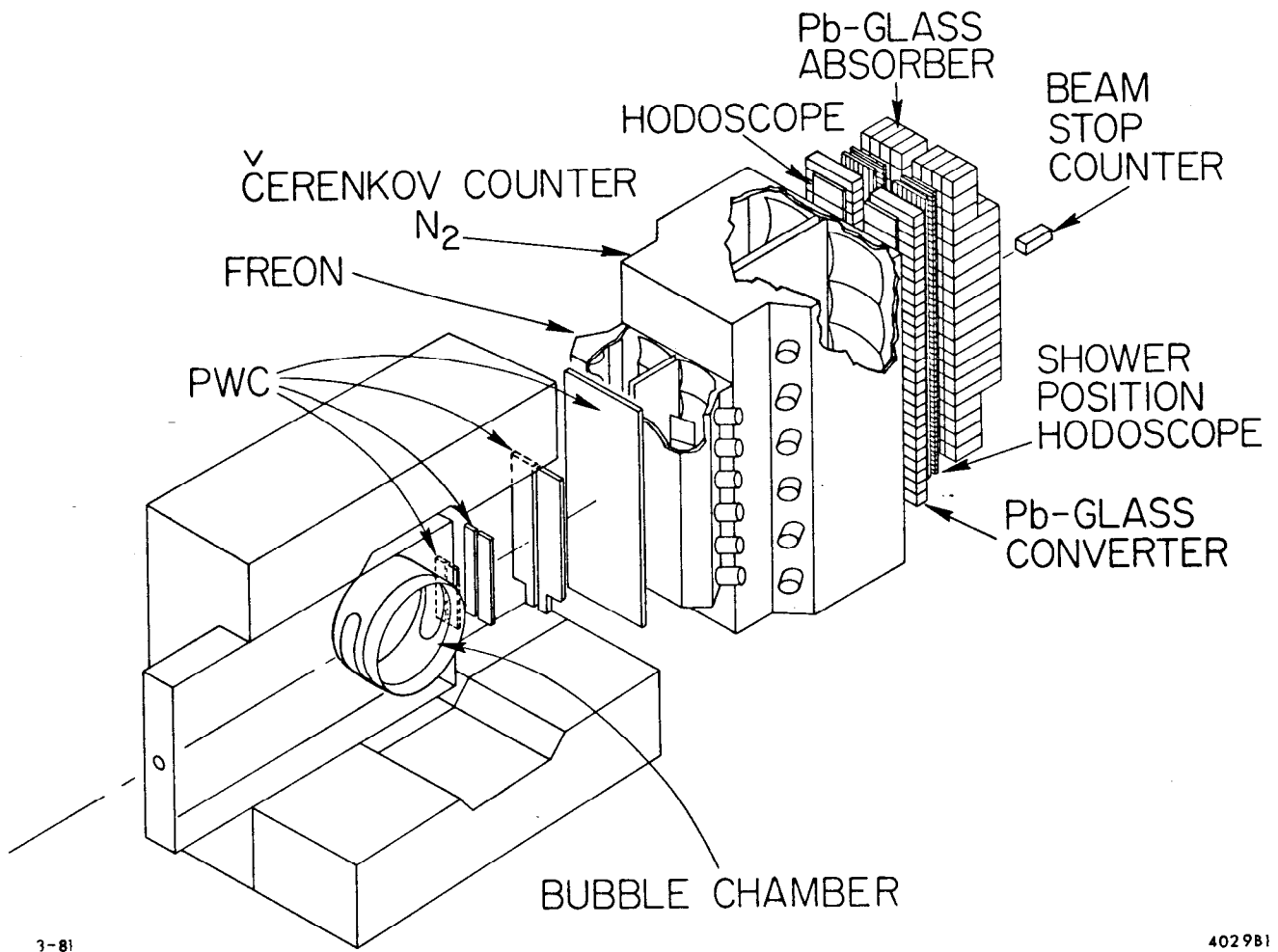


Fig. 2



3-81

402981

Fig. 3

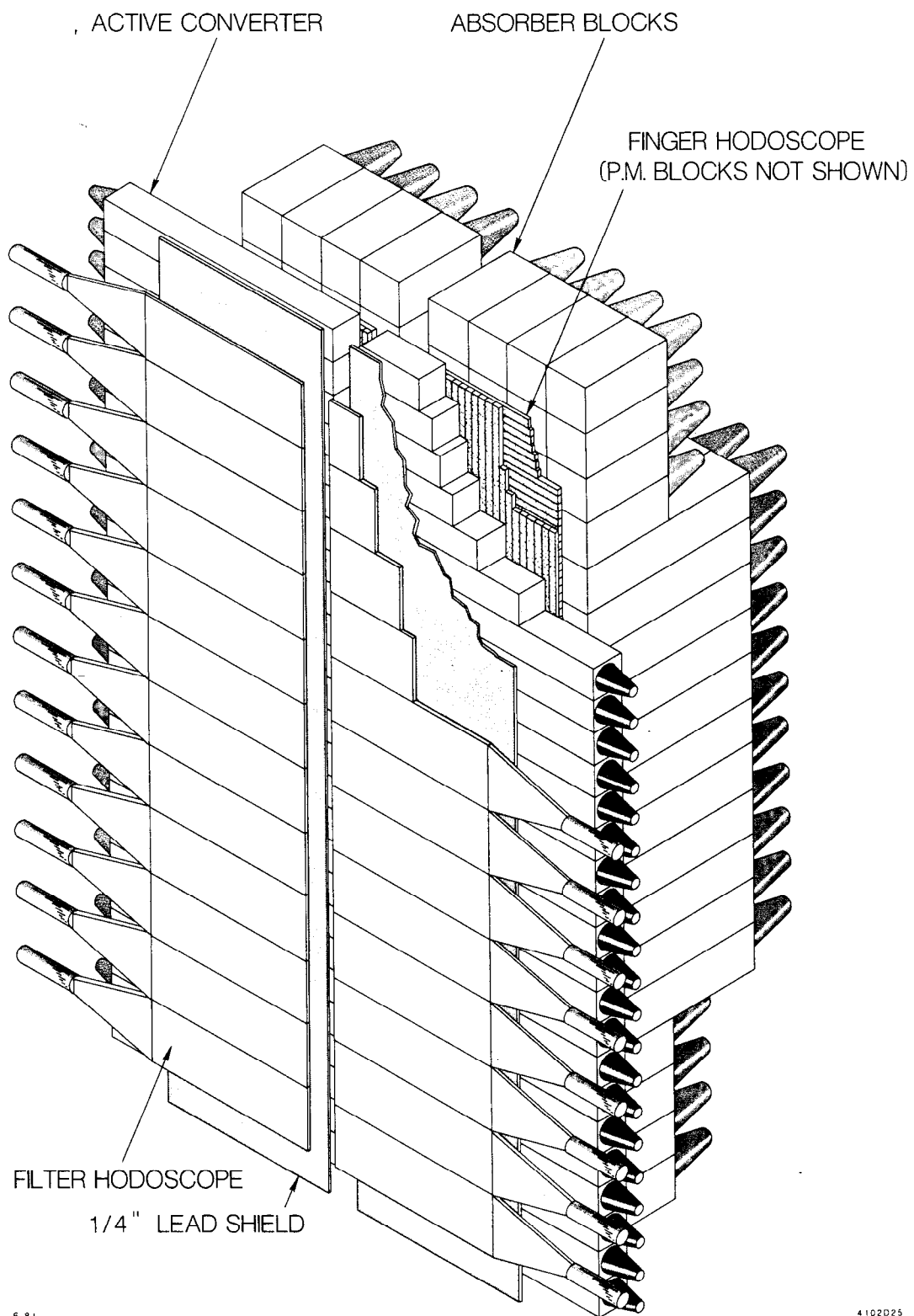


Fig. 4

To Phototubes

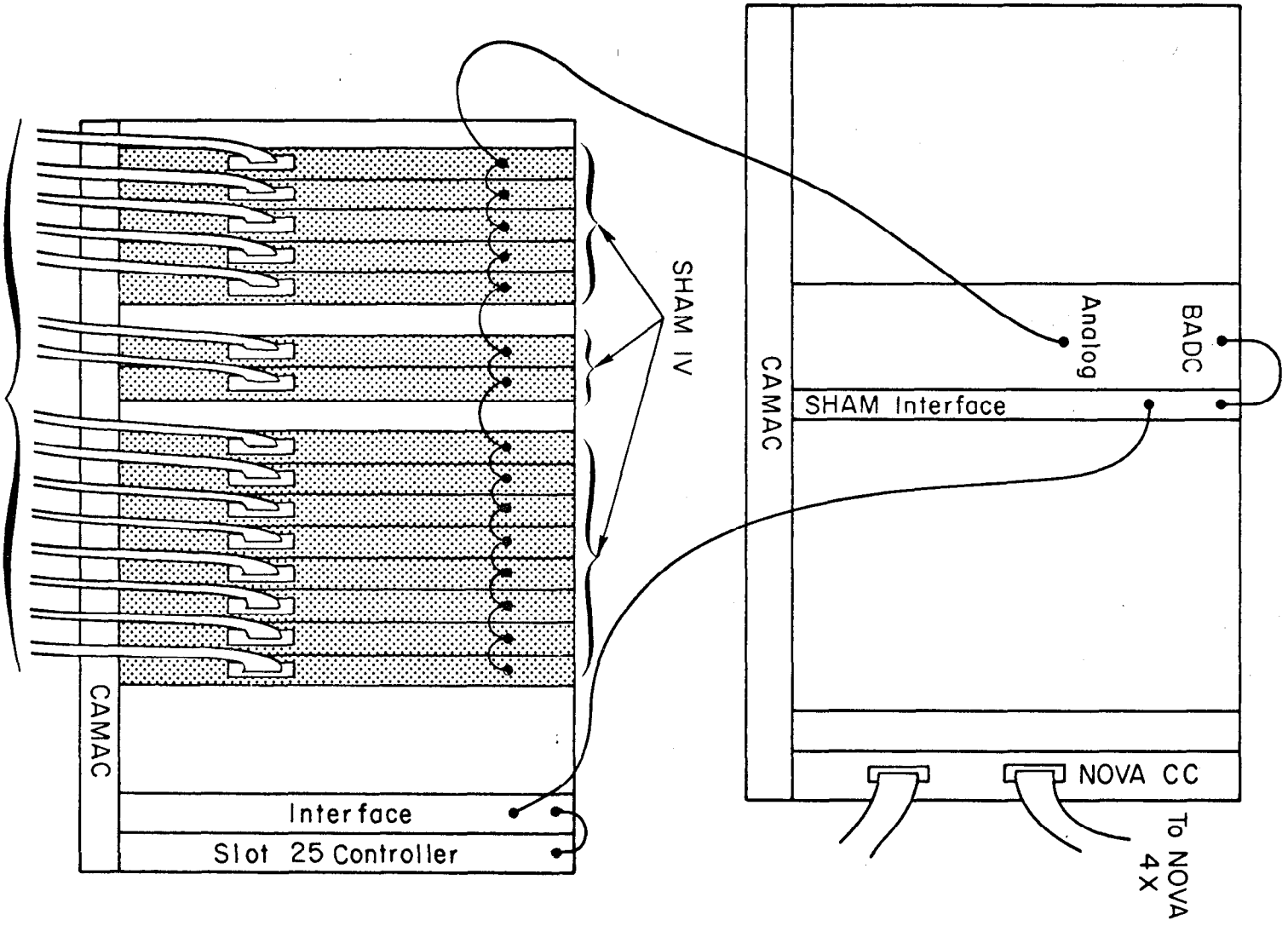
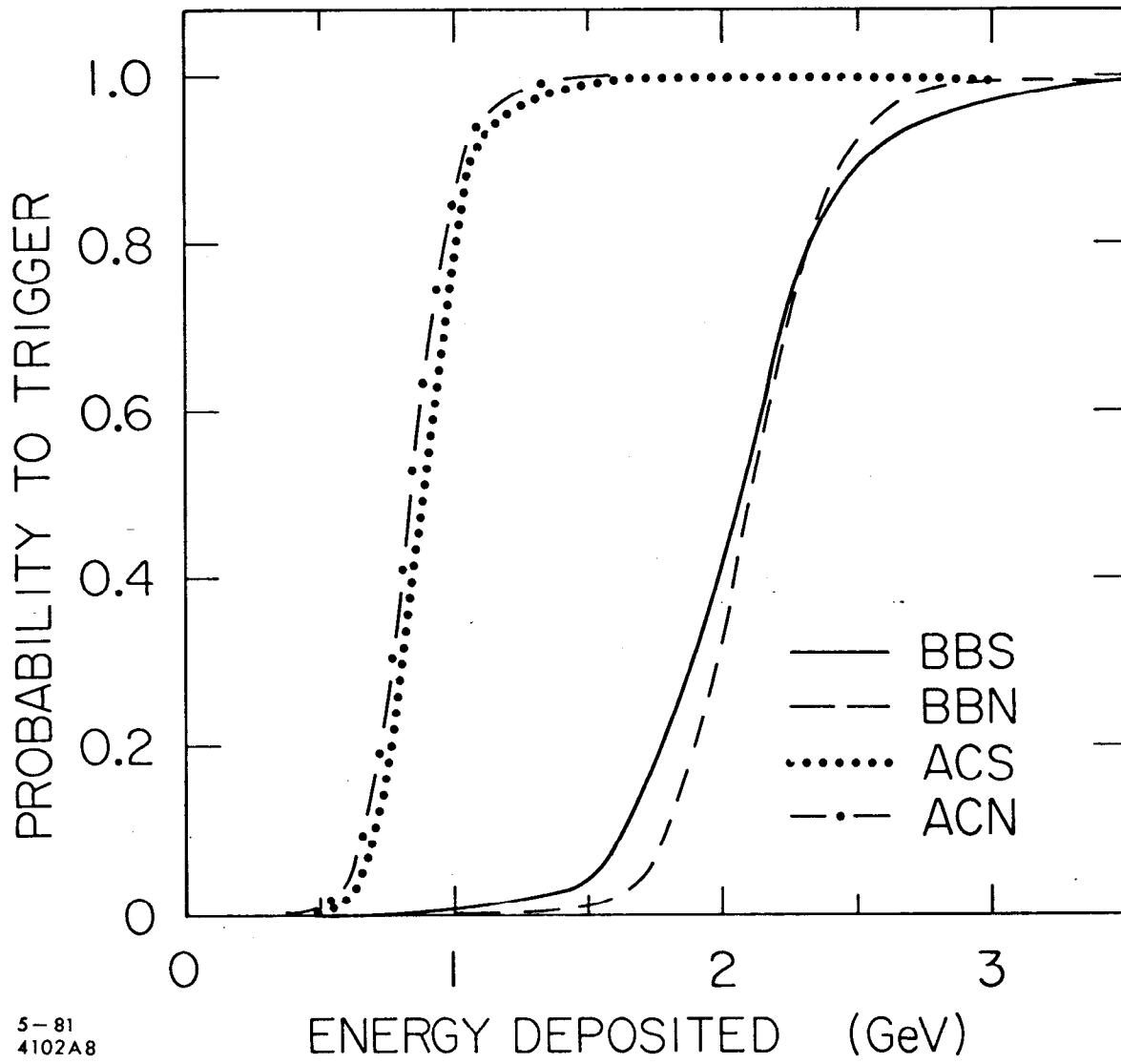


Fig. 5



5-81  
4102A8

Fig. 6



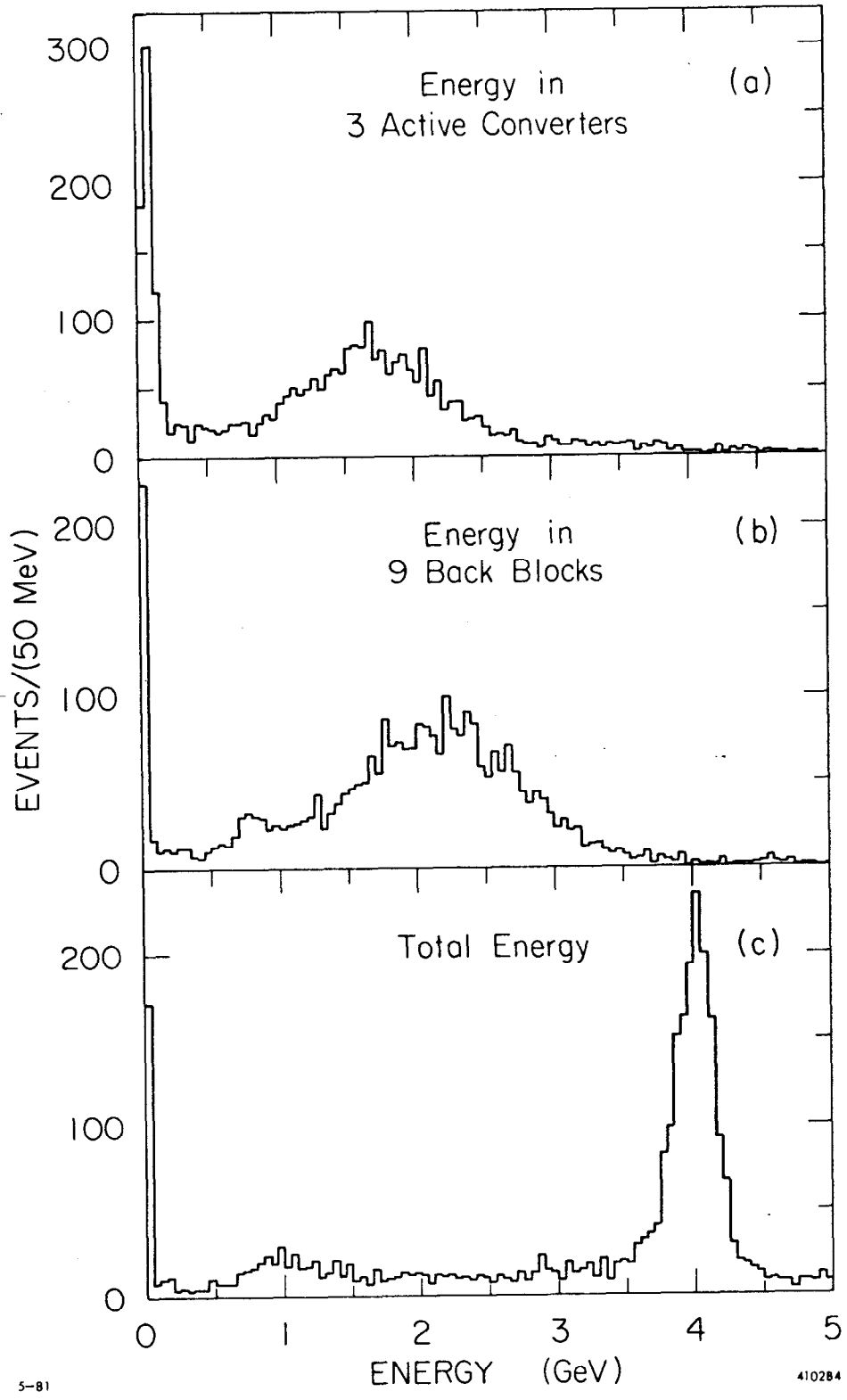


Fig. 8

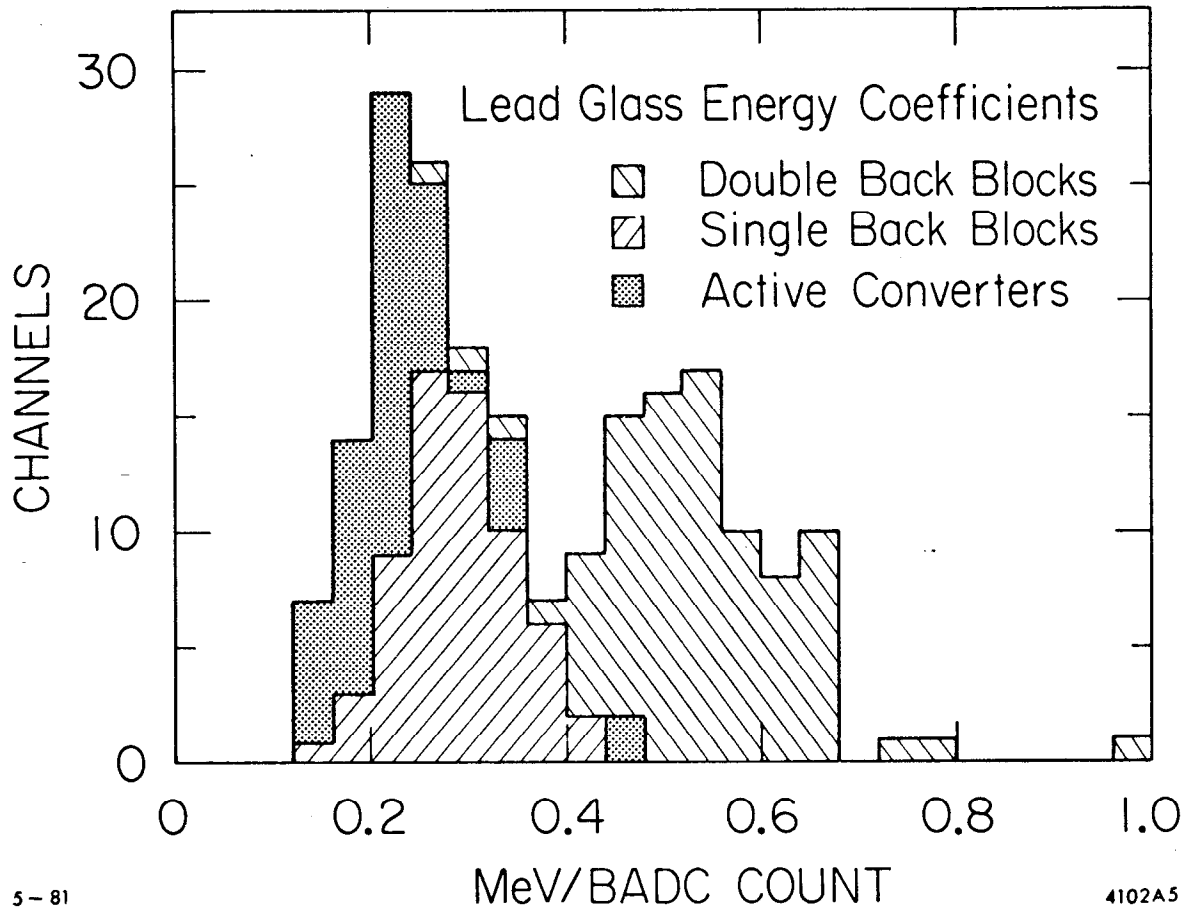
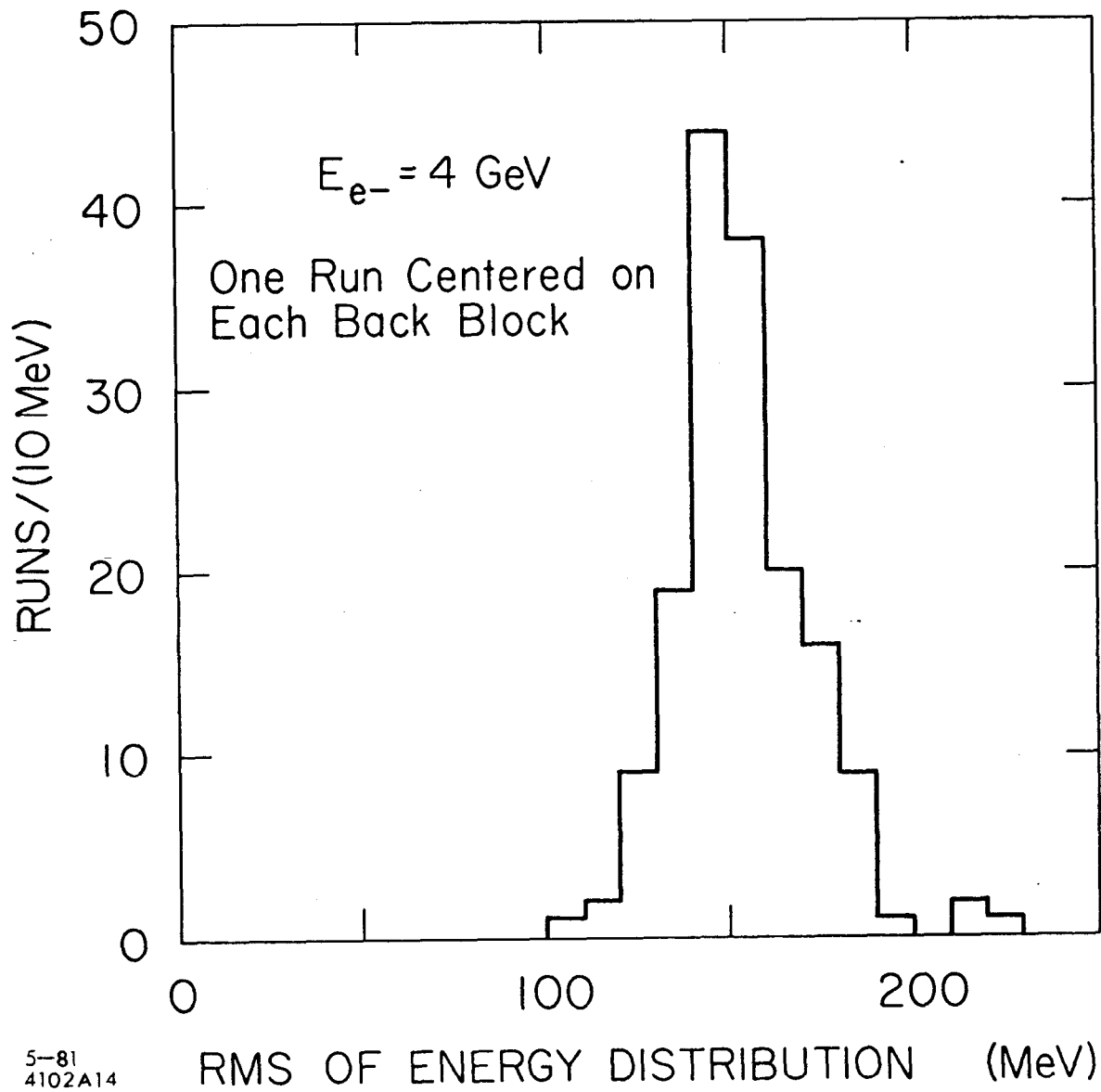
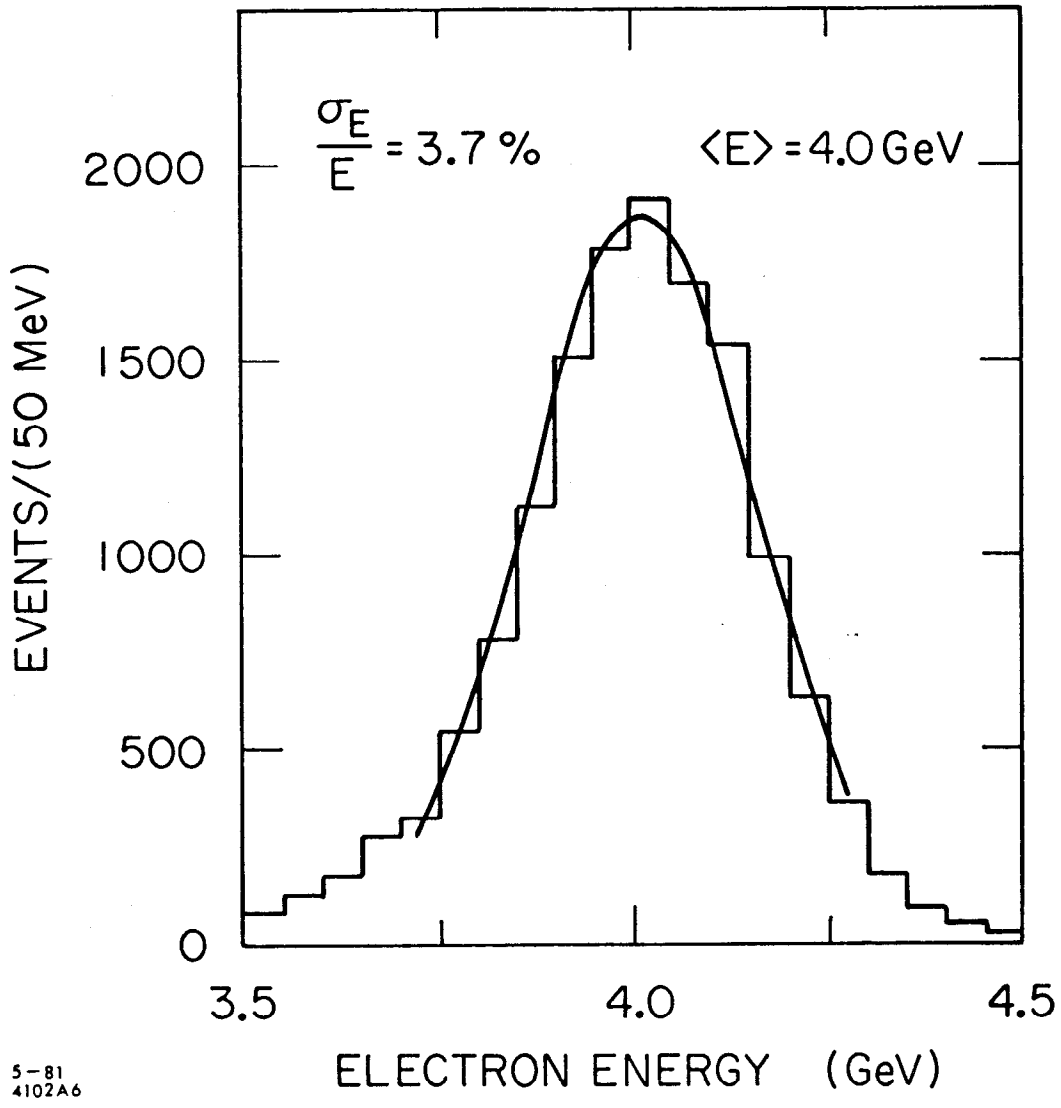


Fig. 9



5-81  
4102A14

Fig. 10



5-81  
4102A6

Fig. 11

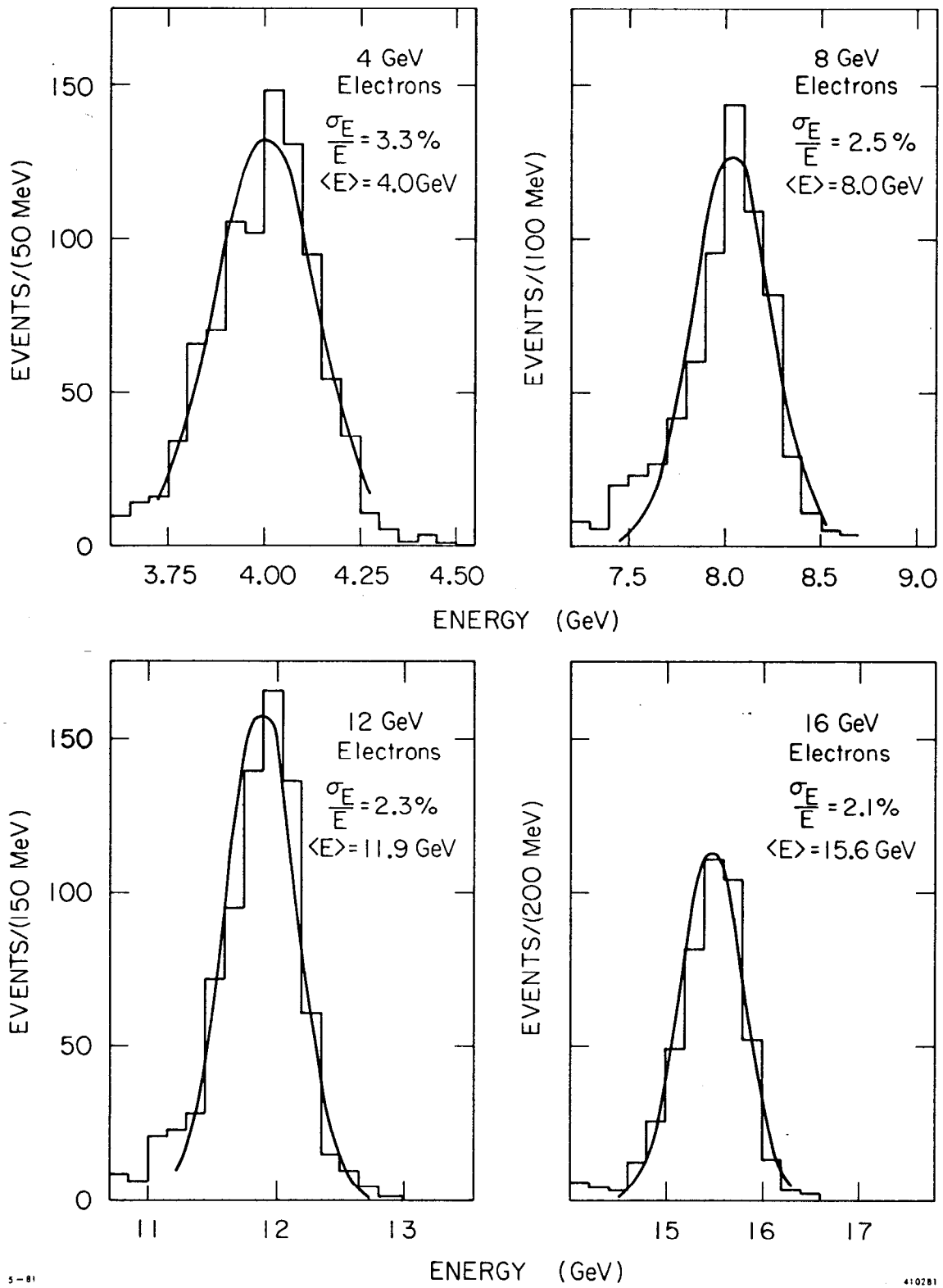


Fig. 12

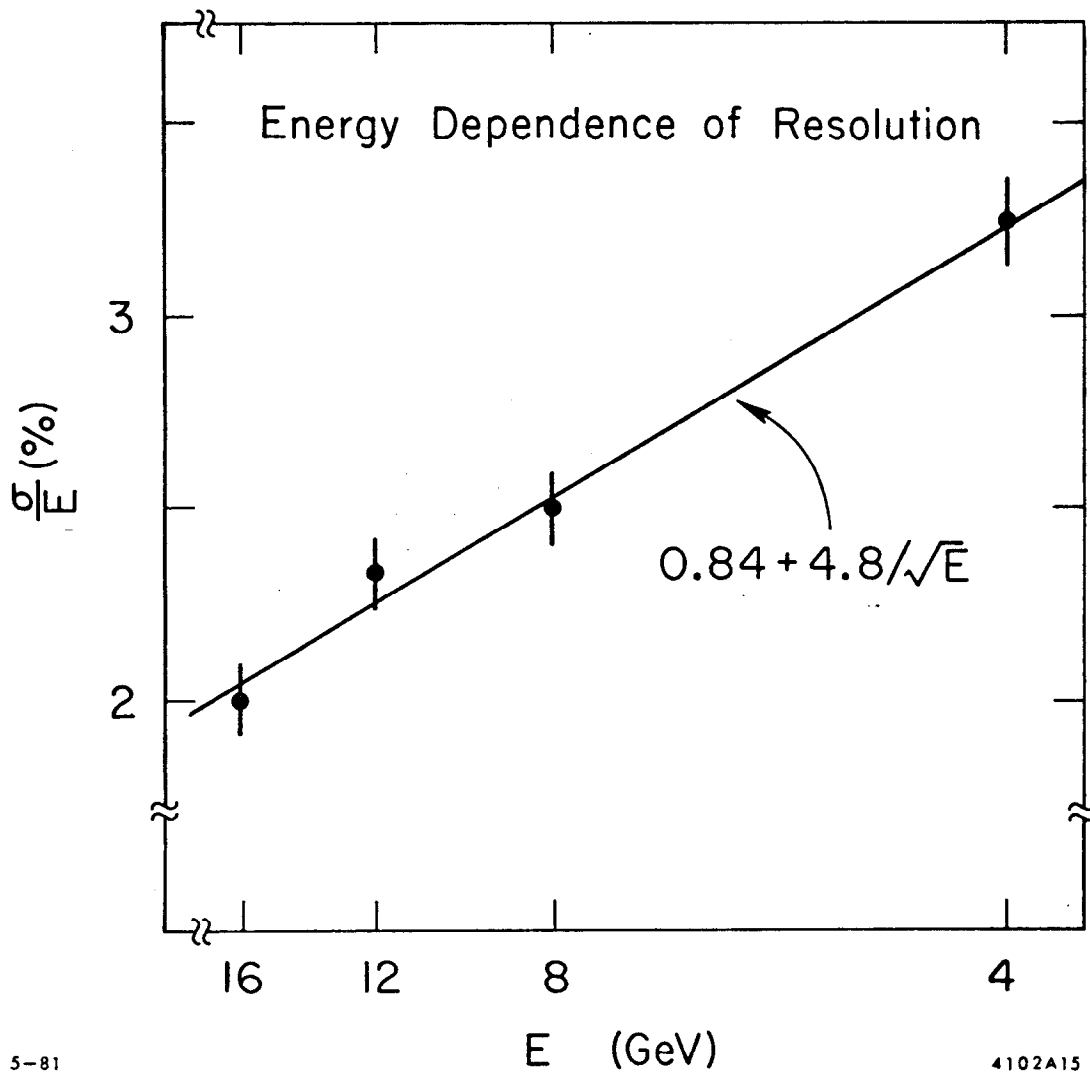
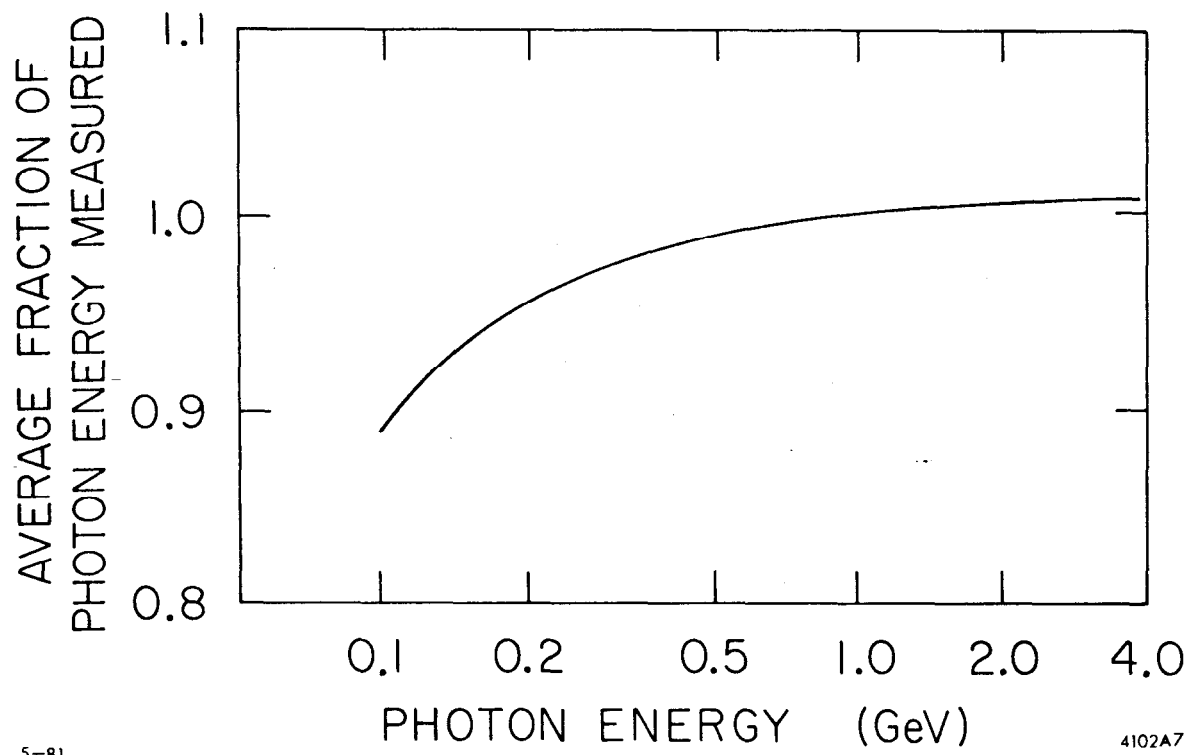


Fig. 13



5-81

4102A7

Fig. 14

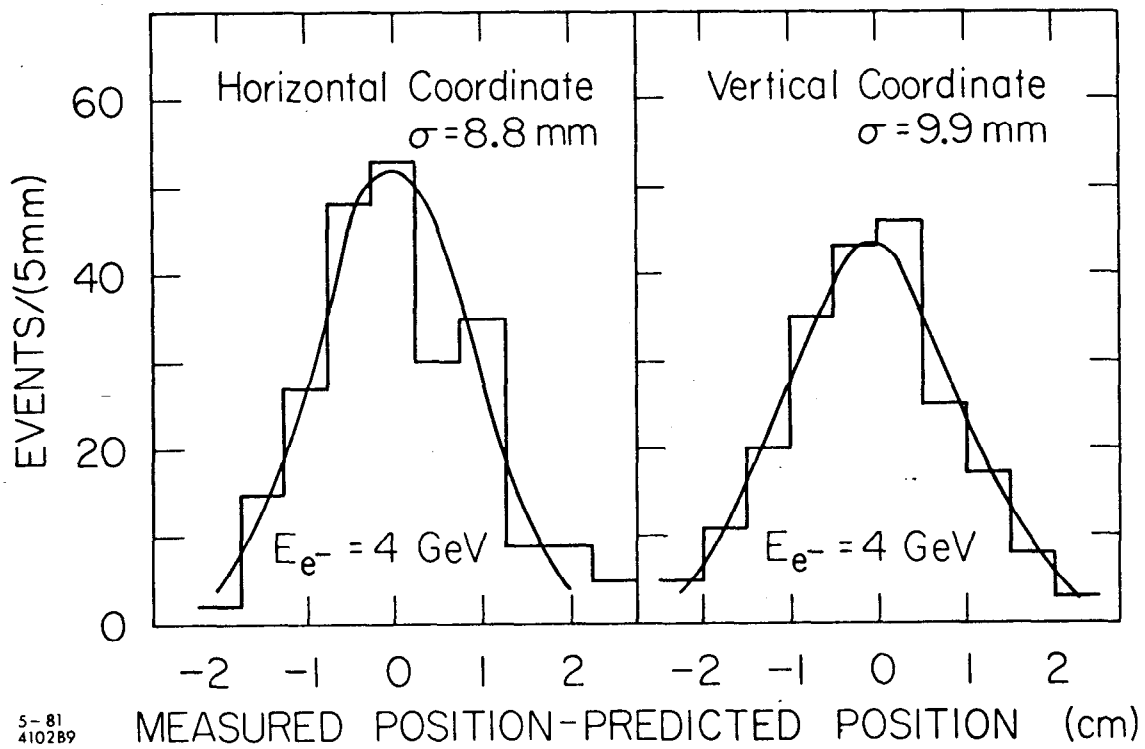
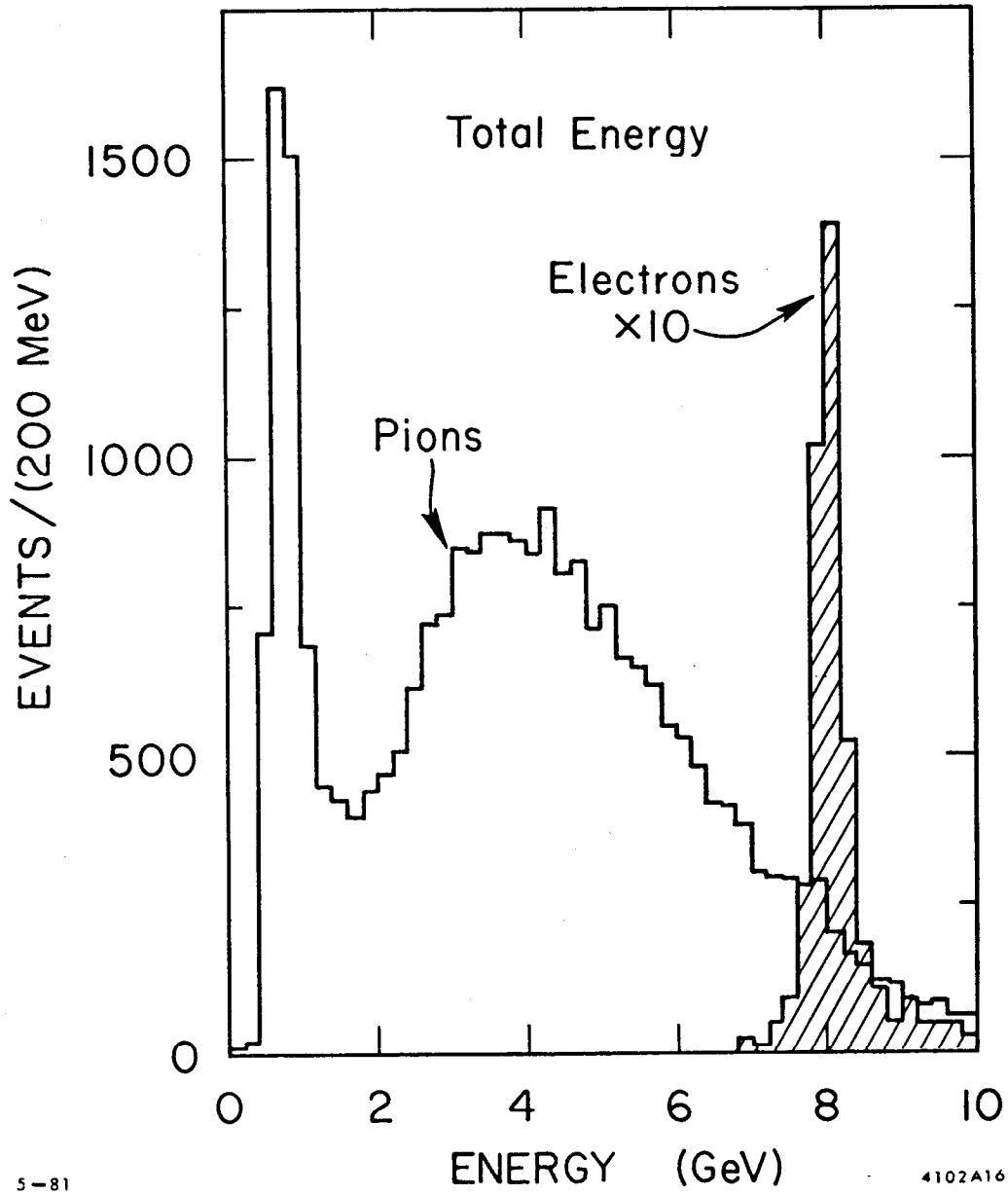


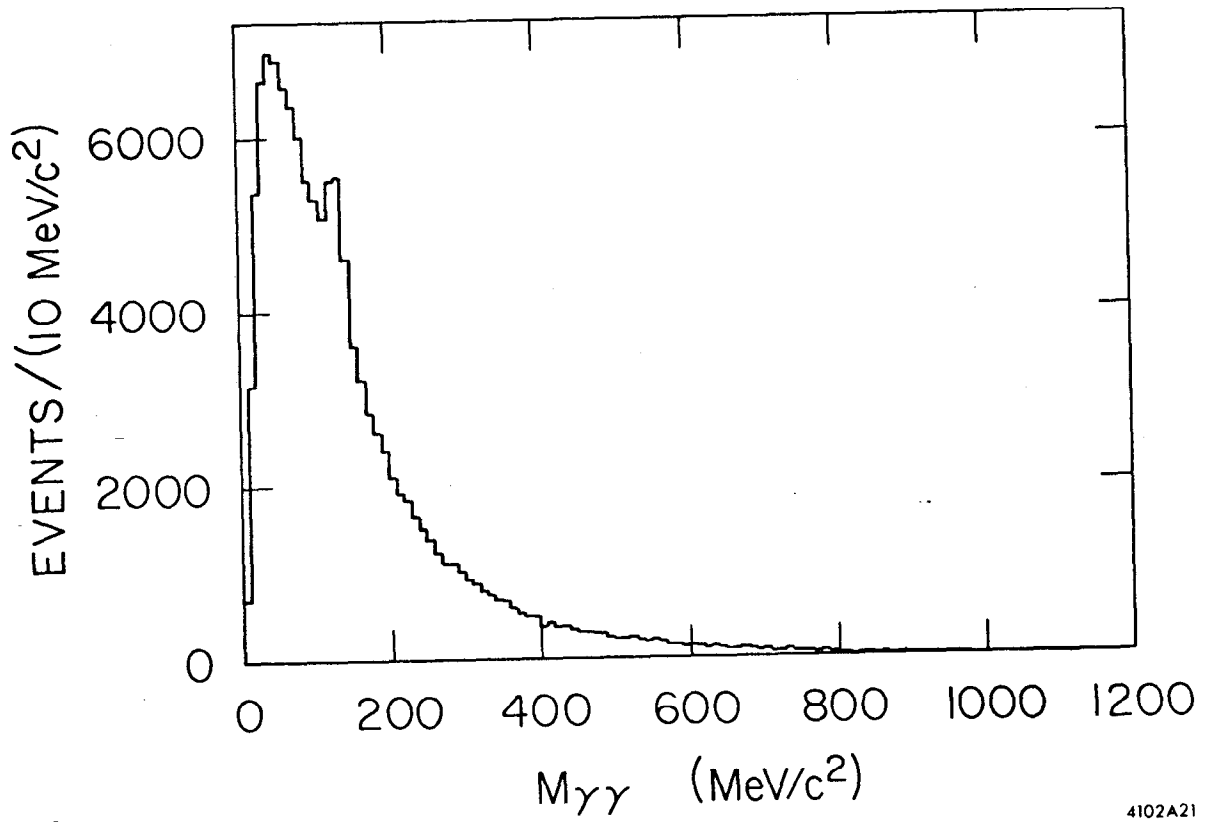
Fig. 15



5-81

4102A16

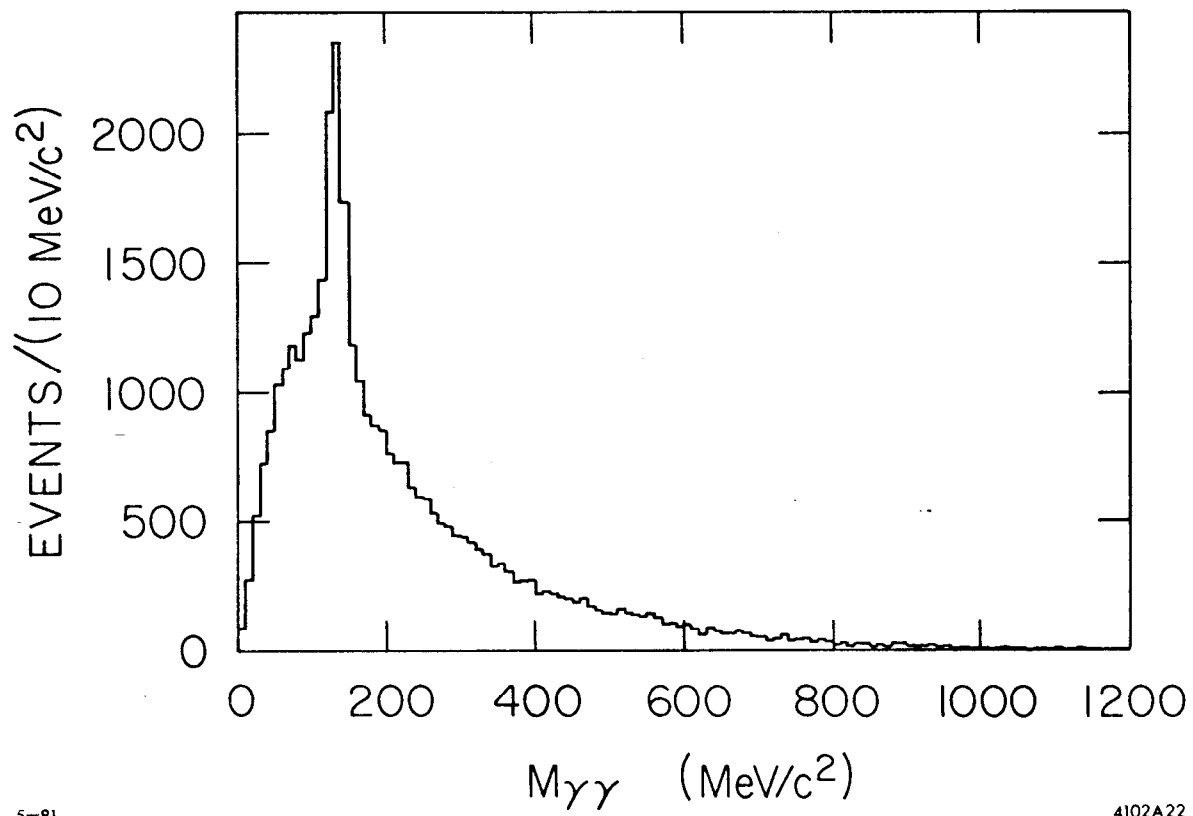
Fig. 16



5-81

4102A21

Fig. 17



5-81

4102A22

Fig. 18

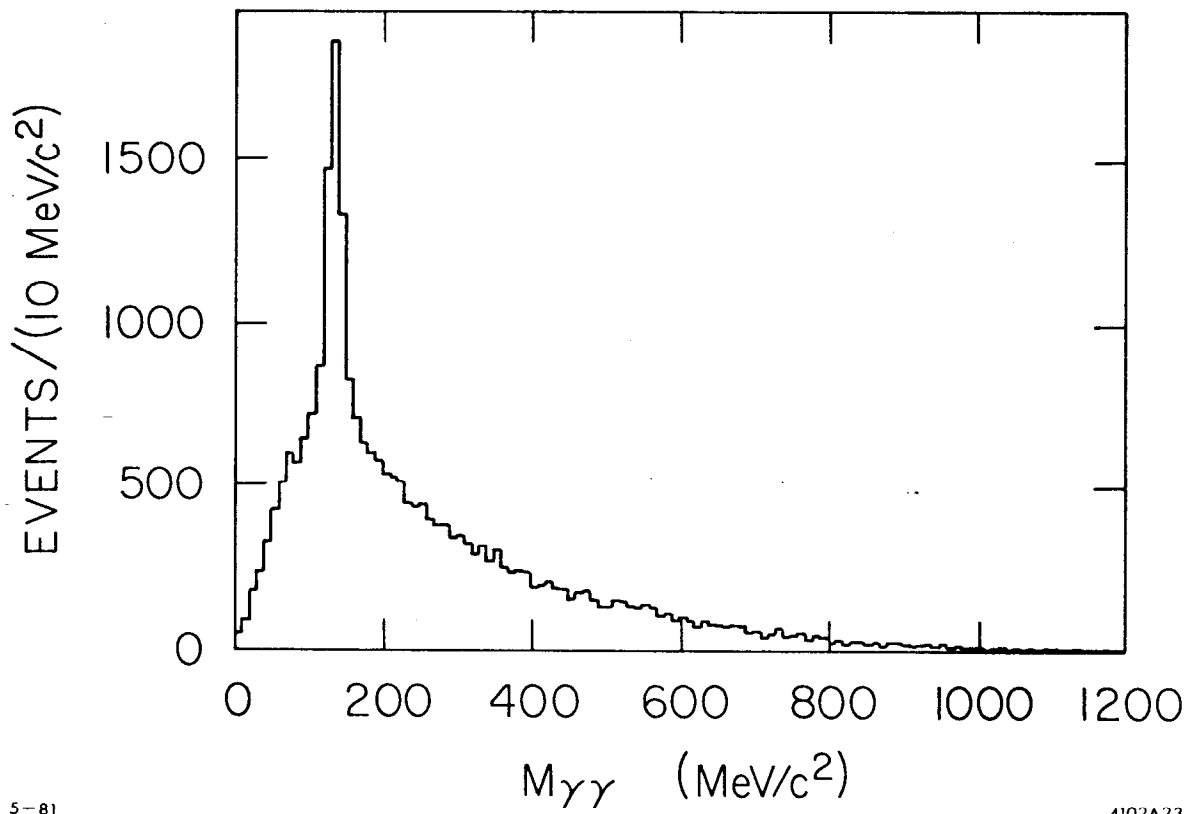
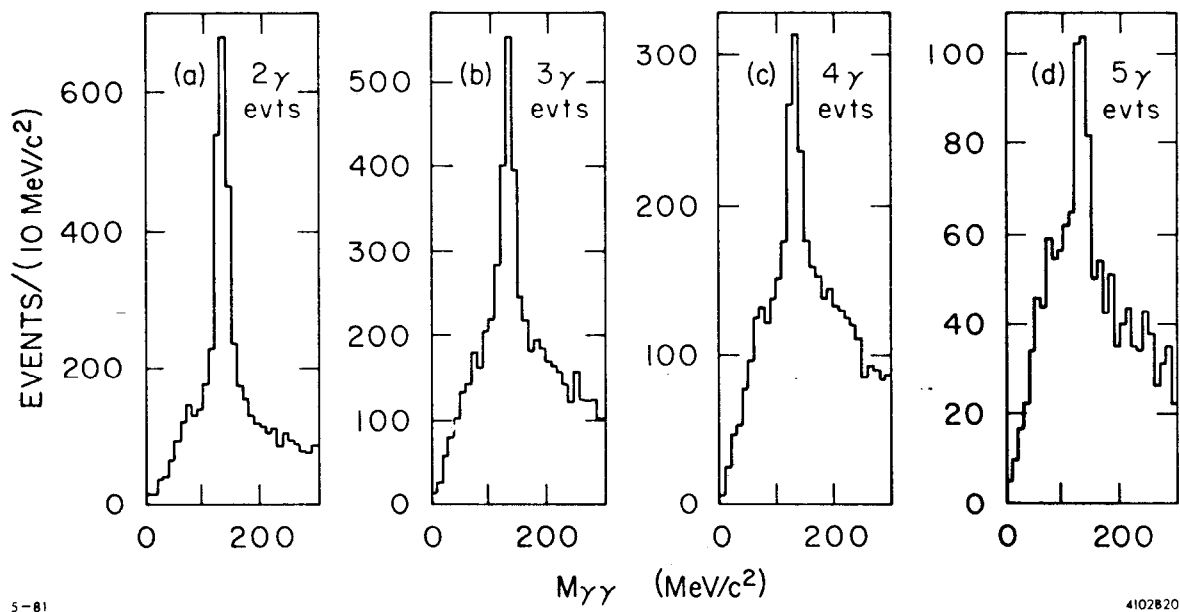


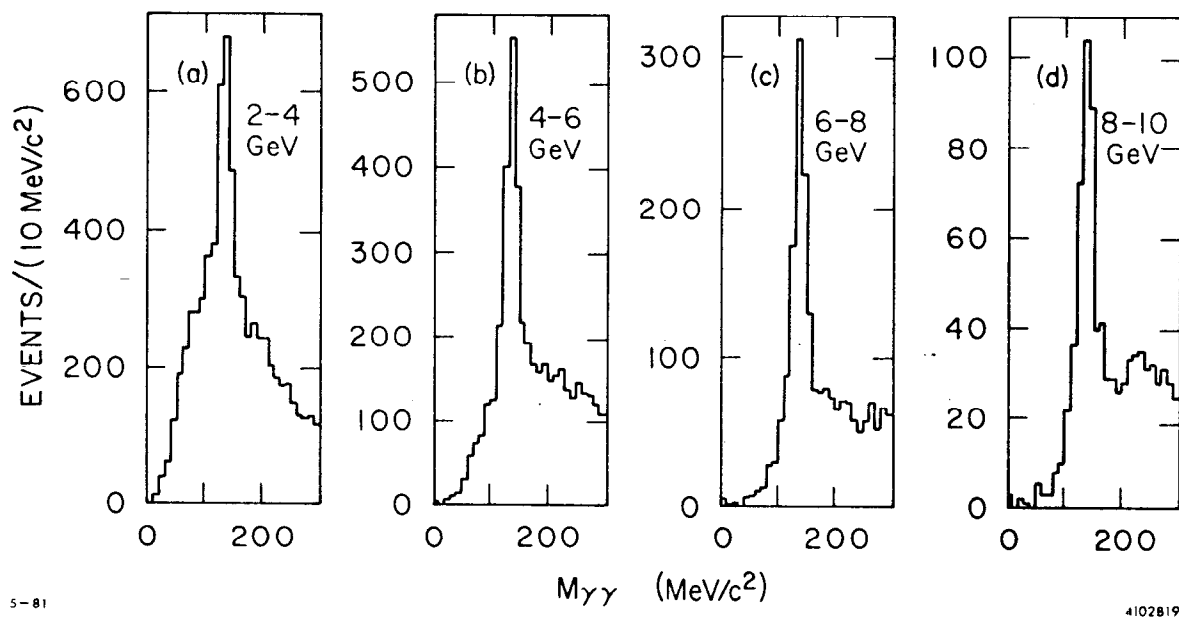
Fig. 19



5-81

4102820

Fig. 20



5-81

4102819

Fig. 21

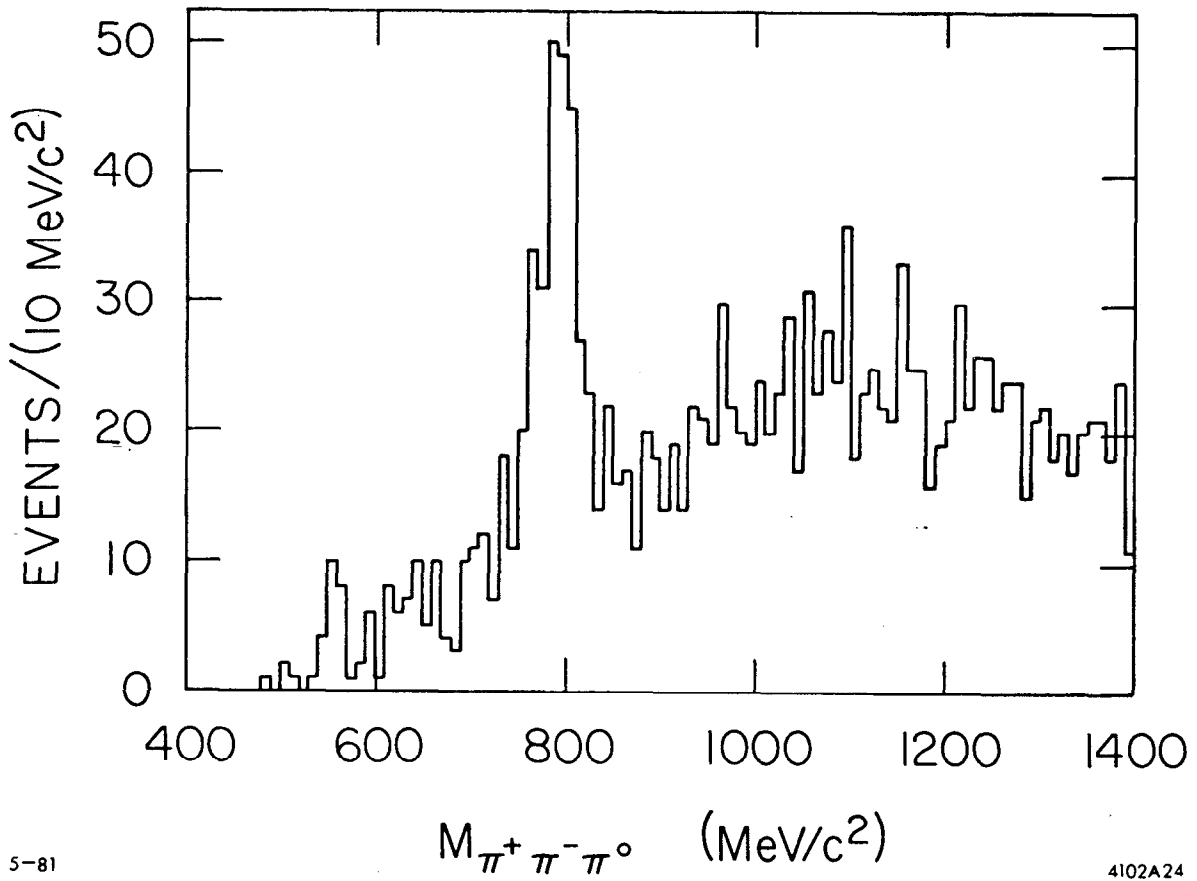


Fig. 22